Dalton Transactions

PAPER

View Article Online
View Journal | View Issue

Open Access Article. Published on 01 July 2016. Downloaded on 10/20/2025 3:45:00 PM.
This article is licensed under a Creative Commons Attribution 3.0 Unported Licence.

Cite this: *Dalton Trans.*, 2016, **45**, 12114

Received 3rd May 2016,
Accepted 1st July 2016

DOI: 10.1039/c6dt01737a

www.rsc.org/dalton

Formation of defect-fluorite structured $NdNiO_xH_y$ epitaxial thin films *via* a soft chemical route from $NdNiO_3$ precursors

T. Onozuka,[a] A. Chikamatsu,*[a] T. Katayama,[a] T. Fukumura[b] and T. Hasegawa[a,c]

A new phase of oxyhydride $NdNiO_xH_y$ with a defect-fluorite structure was obtained by a soft chemical reaction of $NdNiO_3$ epitaxial thin films on a substrate of $SrTiO_3$ (100) with CaH_2. The epitaxial relationship of this phase relative to $SrTiO_3$ could be controlled by changing the reaction temperature. At 240 °C, $NdNiO_xH_y$ grew with a [001] orientation, forming a thin layer of infinite-layer $NdNiO_2$ at the interface between the $NdNiO_xH_y$ and the substrate. Meanwhile, a high-temperature reaction at 400 °C formed [110]-oriented $NdNiO_xH_y$ without $NdNiO_2$.

Introduction

The topotactic reaction of transition-metal oxides with metal hydrides is utilized as a facile and efficient synthesis approach for novel or mixed-anion oxides.[1,2] In this class of reaction, metal hydrides can act as either strong reducing reagents for removing oxide anions or incorporating hydride anions. Reactions with the former role yield transition-metal oxide phases with exceptionally low oxidization states (Ni^+, Ru^{2+}, Co^+),[3–7] unusual coordination networks (square-planar Fe^{2+}),[8] or both, while those with the latter allow the preparation of oxyhydrides[9–11] such as $LaSrCoO_3H_{0.7}$, $BaTiO_{3-x}H_x$, and $SrVO_2H$. Topotactic reactions can be performed at low reaction temperatures; for example, a typical reaction temperature during oxygen deintercalation or hydride ion incorporation is below 500 °C,[3–10] which is considerably lower than those of conventional "hard" solid-state reactions (~1000 °C). Reactions at these low temperatures, classified as "soft" chemical reactions, enable the synthesis of metastable compounds, such as oxyhydrides, that can decompose easily at elevated temperatures.

Although topotactic reactions are typically used to produce powdered samples, several groups have applied the metal-hydride reaction to thin films, reporting fabrications of $LaNiO_2$,[12,13] $SrFeO_2$,[14] $Sr_{1-x}Eu_xFeO_2$,[15] $ATiO_{3-x}H_x$ [16] (A = Ca, Ba, or Sr), $SrCoO_xH_y$,[17] and $LaSrCoO_{4-x}H_x$ [18] as thin films. The topotactic reaction of epitaxial thin films allows the preparation of single-crystalline films, which can be used to measure the intrinsic physical properties of materials. In addition, the concentration of the introduced heteroatoms can be much higher in films than in bulk samples because of the higher reactivity of thin films. Katayama *et al.*[19] recently reported that a $SrFeO_2$ thin film, obtained by a topotactic reaction between $SrFeO_{2.5}$ and CaH_2, contained a significant amount of hydrogen (~3×10^{21} atoms per cm^3). The hydrogen could serve as an electron acceptor and generate metallic conductivity, in contrast to bulk $SrFeO_2$.

Here, we investigate the topotactic reaction of perovskite $NdNiO_3$ epitaxial thin films with CaH_2. Perovskite $NdNiO_3$ shows a metal–insulator transition at 200 K (ref. 20) associated with charge ordering and a structural transition.[21] The reduction of $NdNiO_3$ powder using metal hydrides was reported to yield infinite-layer $NdNiO_{2+x}$,[3,4] although the presence of hydrogen in the reduced product was not confirmed. In this study, we found that the CaH_2 treatment of $NdNiO_3$ epitaxial thin films completely altered the cation framework, producing defect-fluorite-structured $NdNiO_xH_y$. Moreover, the growth orientation of the defect-fluorite phase changed as a function of the reaction temperature with CaH_2.

Experimental methods

Epitaxial $NdNiO_3$ thin films were deposited as precursors onto $SrTiO_3$ (STO) (100) substrates (Shinkosha Co., Ltd) by pulsed laser deposition (PLD) at a substrate temperature of 650 °C, an oxygen partial pressure of 13 Pa, a laser (KrF excimer, 248 nm wavelength) fluence of 2 J cm^{-2}, and a repetition rate of 5 Hz. The obtained precursor films were then reacted with CaH_2 powder (Wako Pure Chemical Industries, Ltd) in a Pyrex tube evacuated with a rotary pump. The reaction temperature and

[a]Department of Chemistry, The University of Tokyo, Bunkyo-ku, Tokyo 113-0033, Japan. E-mail: chikamatsu@chem.s.u-tokyo.ac.jp
[b]Department of Chemistry, Tohoku University, Sendai, Miyagi 980-8578, Japan
[c]Kanagawa Academy of Science and Technology (KAST), Kawasaki, Kanagawa 213-0012, Japan

This journal is © The Royal Society of Chemistry 2016

Open Access Article. Published on 01 July 2016. Downloaded on 10/20/2025 3:45:00 PM.
This article is licensed under a Creative Commons Attribution 3.0 Unported Licence.

reaction time were varied in the ranges of 240–400 °C and 1–24 h, respectively. After the reaction, the film was ultrasonically washed with 2-butanone to remove residual powders from the surface. The crystal structures of the samples were characterized by X-ray diffraction (XRD, Bruker AXS D8 Discover) with Cu Kα radiation, as well as by high-angle annular dark-field scanning transmission electron microscopy (HAADF-STEM, Hitachi High-Technologies Co., HD-2700). The amount of hydrogen within the films was measured by dynamic secondary-ion mass spectrometry (SIMS, ULVAC-PHI PHI-ADEPT1010, primary ion: Cs^+, secondary ion: H^-, acceleration voltage: 1.0 kV, detection limit: 1×10^{19} cm^{-3}, depth resolution: ~3 nm).

Results and discussion

Fig. 1a shows the out-of-plane 2θ–θ XRD patterns of the precursor $NdNiO_3$ film on the STO (100) substrate and the film after reaction with CaH_2 at 240 °C for 12 h. The pattern of the precursor films shows the 002 diffraction peak of perovskite $NdNiO_3$ at 2θ = 48.05°. The out-of-plane lattice constant c is calculated as 3.78 Å, in good agreement with the previously reported values.[22,23] Reciprocal space mapping (RSM) around the 103 asymmetric diffraction (Fig. 1b) reveals that the in-plane lattice of the $NdNiO_3$ (a-axis) is completely locked to the STO substrate. The in-plane lattice constant is larger than the out-of-plane one, indicating that the film is under in-plane tensile strain from the substrate. Meanwhile, in the 2θ–θ pattern of the film treated with CaH_2 (Fig. 1a), the peak from $NdNiO_3$ has completely disappeared; a new peak at $2\theta \approx 55.8°$ (d = 1.65 Å) has emerged, which corresponds to the 002 diffraction of infinite-layer $NdNiO_2$. In RSM (Fig. 1c), the $NdNiO_2$ 103 peak is located just above that of STO 103, demonstrating that the epitaxial relationship between the film and the substrate is maintained during the chemical reaction with CaH_2. However, the intensity of the $NdNiO_2$ 002 diffraction is much weaker than that in the pattern of the precursor film. Furthermore, in the RSM image, the diffraction spot is significantly elongated along the q_z direction. These changes suggest that $NdNiO_2$ exists as a very thin layer within the film.

To obtain further information on the crystal structure, we performed atomic-level HAADF-STEM imaging of the CaH_2-treated film. Fig. 2a shows a large area (~200 nm width) HAADF image of the CaH_2-treated film, indicating almost no contrast. Since the brightness of HAADF images depends on the atomic number of the constituent elements, the lack of contrast indicates that neodymium and nickel are homogeneously distributed in the film with no cation segregation. Fig. 2b is a high-resolution image taken near a film/substrate interface. In the region near the substrate (Region ii), a rectangular lattice with (a, c) = (3.9 Å, 3.3 Å), representing c-axis oriented $NdNiO_2$, is observed. The thickness of this region is approximately ten monolayers; this explains the weakness and breadth of the $NdNiO_2$ diffraction peak in Fig. 1. Fig. 2b also indicates the presence of a thin interfacial layer measuring ~0.5 nm in thickness (Region i). A similar interfacial layer was observed in infinite-layer $Sr_{0.9}La_{0.1}CuO_2$ thin films grown by molecular-beam epitaxy;[24] it was proposed to promote the growth of the infinite-layer phase.

Meanwhile, the atomic arrangement in Region iii, located above Region ii and occupying most of the film, is completely

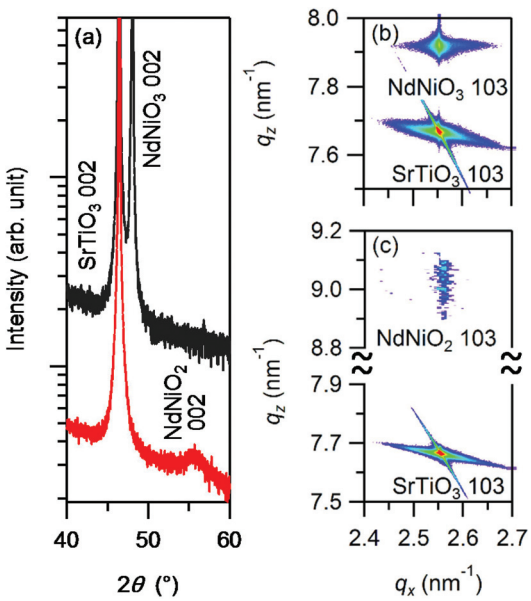

Fig. 1 (a) XRD 2θ–θ patterns before (black) and after (red) the reaction with CaH_2 at 240 °C. Reciprocal space maps (b) before and (c) after the reaction.

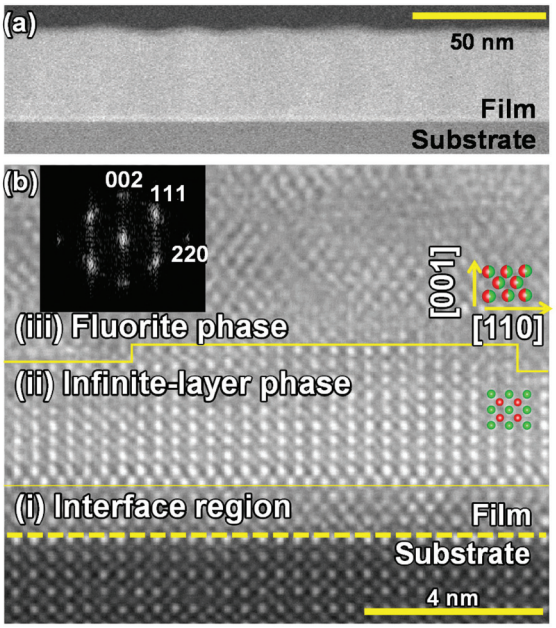

Fig. 2 (a) Wide and (b) magnified view of HAADF-STEM images after the reaction at 240 °C for 12 h. Inset: Fourier transform of the fluorite phase region (iii). Green and red circles show the positions of neodymium and nickel atoms, respectively.

Open Access Article. Published on 01 July 2016. Downloaded on 10/20/2025 3:45:00 PM.
This article is licensed under a Creative Commons Attribution 3.0 Unported Licence.

different from that of $NdNiO_2$: each atom in Region iii is imaged with a contrast brighter than that of nickel but darker than that of neodymium in Region ii. This suggests that the metals are randomly distributed in Region iii. The lattice image in Region iii can be understood by assuming a face-centered cubic (fcc) lattice viewed along the [110] direction, as depicted by the green and red points in the figure. From the Fourier transform of the HAADF image (inset in Fig. 2b), the lattice constant is estimated as 5.5 Å. The observed atomic arrangement and lattice constant are near those of a fluorite-structured oxyhydride, NdHO[25] (a = 5.61 Å in pseudocubic notation). Therefore, we tentatively conclude that the reaction of $NdNiO_3$ with CaH_2 yields a fluorite-structured NdHO-related phase as a major component of the film; hereafter, this is called the fluorite phase.

In order to determine the chemical composition of this NdHO-related fluorite film, we performed dynamic SIMS and EDS measurements. Fig. 3a shows a hydrogen depth profile measured by SIMS for the sample treated with CaH_2 at 240 °C, clearly indicating that hydrogen is homogeneously distributed in the film. The hydrogen density is evaluated as $\sim 9 \times 10^{21}$ atoms per cm^3 (0.7 per formula unit, fu), although this has some uncertainty because hydrogen-implanted STO was used as a standard reference. The hydrogen density in the substrate was more than one order of magnitude smaller than that in the film. Fig. 3b plots the differential secondary-ion intensities of strontium, titanium, neodymium, nickel, and hydrogen. As observed, the hydrogen density abruptly drops at a position several nanometers shallower than the film–substrate interface. This indicates that hydrogen is mainly incorporated into the fluorite phase, rather than the infinite-layer $NdNiO_2$.

Fig. 3c compares the EDS spectra of the film before and after the reaction with CaH_2. The nickel/neodymium ratio remains constant, whereas the intensity of the O Kα peak is suppressed by 20% after the reaction. Assuming that the peak intensity of each element is proportional to its concentration, the oxygen density is estimated as 2.3/fu. From these results, the chemical formula of the fluorite phase is estimated as $NdNiO_xH_y$ with $(x, y) \approx (2.3, 0.7)$. The total anion (oxygen + hydrogen)/cation (neodymium + nickel) ratio is approximately 3/2, smaller than the ideal value of 2, which suggests that the obtained oxyhydride phase has a defect-fluorite structure.

Finally, we describe the selective synthesis of the oxyhydride phase *via* a solid-phase reaction with CaH_2 at higher temperature. Fig. 4a and b show the out-of-plane (χ = 90°) and asymmetric (χ = 35°) XRD patterns of the film prepared at 400 °C. Notably, the former indicates no peaks assignable to the infinite-layer $NdNiO_2$ phase, whereas a clear peak from the fluorite oxyhydride phase is observed in the latter, demonstrating the formation of a phase-pure oxyhydride phase without infinite-layer $NdNiO_2$. The peak at 2θ = 28° in Fig. 4b is assignable to the 111 diffraction of the fluorite phase. This implies that the oxyhydride film heat-treated at 400 °C is [110]-oriented, in contrast to the film prepared at 240 °C with the [001]-orientation. A HAADF-STEM measurement also confirms this orientation change. Most of the film consisted of the [110]-oriented crystals (as in Fig. 4c), while the crystals adjacent to the substrate–film interface (2–3 nm thick, Fig. 4d) remained [001]-oriented. Additionally, SIMS measurement

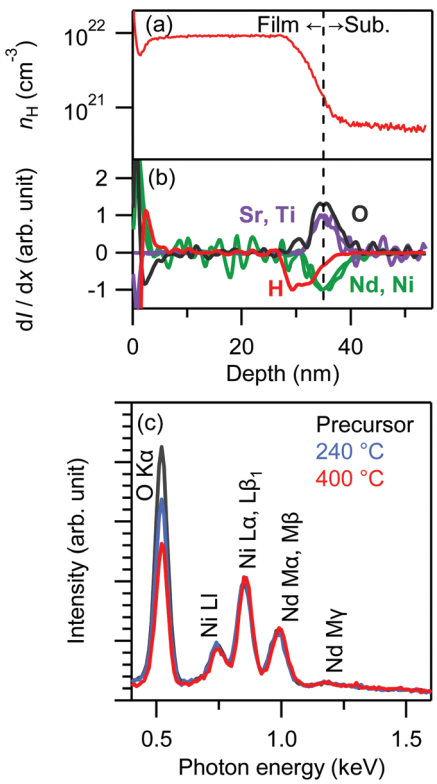

Fig. 3 (a) Depth dependence of atomic hydrogen density (n_H) after the reaction at 240 °C. (b) Differential secondary-ion intensity (dI/dx) of each element. (c) EDS spectra of the films before (black) and after the reaction (blue, red), measured at an acceleration voltage of 2.5 kV.

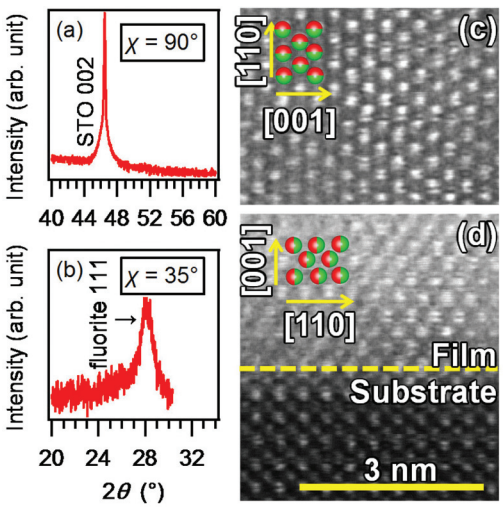

Fig. 4 (a) Out-of-plane (χ = 90°) and (b) asymmetric (χ = 35°) XRD patterns of the films reacted at 400 °C for 24 h. HAADF-STEM images of the film reacted at 400 °C for 24 h (c) at the middle of the film and (d) at the interface between the film and the substrate.

 This journal is © The Royal Society of Chemistry 2016

Open Access Article. Published on 01 July 2016. Downloaded on 10/20/2025 3:45:00 PM.
This article is licensed under a Creative Commons Attribution 3.0 Unported Licence.

revealed that this sample contained 6×10^{21} cm^{-3} of hydrogen (0.5/fu), comparable to that of the sample prepared at the lower temperature of 240 °C (0.7/fu). The EDS measurement confirmed that the neodymium and nickel contents in this film were invariant after the heat-treatment, while the oxygen content decreased from 2.3 (at 240 °C) to 1.7 (at 400 °C). If hydrogen is present as H^-, H, or H^+, the nominal valence state of nickel is calculated to be +0.9, +0.4, or −0.1, respectively. Though +3 (as in $NdNiO_3$), +2 (as in NiO), and +1 (as in $NdNiO_2$) states of nickel are known in extended oxides, to the best of our knowledge, there are no reports on zero or negative charge states of nickel oxides. Therefore, it seems natural to assume that hydrogen exists as hydride anions rather than protons or charge-neutral atoms.

In the [001]-oriented fluorite film obtained at 240 °C, the [110] and [1−10] axes of $NdNiO_xH_y$ are parallel to the [100] and [010] directions of the STO substrate, respectively. The cubic lattice constant a of the substrate (3.905 Å) and $a/\sqrt{2}$ of the fluorite phase (≈3.9 Å) are nearly equal; thus, it is natural that [001]-orientated fluorite is grown on STO (100). Meanwhile, the orientation change mentioned above is contrary to our prediction based on the epitaxial relationship between the fluorite film and the substrate. In the [110]-oriented $NdNiO_xH_y$ film obtained at 400 °C, the [1−10] and [001] axes are parallel to the [100] and [010] directions of the substrate, respectively. In this orientation, the in-plane lattice of $NdNiO_xH_y$ has a rectangular shape with axes of 3.9 Å (along $[100]_{substrate}$) and 5.5 Å (along $[010]_{substrate}$). The latter value is incommensurable with that of the substrate and thus the [110]-oriented $NdNiO_xH_y$ film is expected to have a lattice match poorer than that of the [001]-oriented crystal. A similar orientation change was reported in $LaNiO_2$ thin films obtained by the topotactic reduction of $LaNiO_3$, in which c-axis-orientated $LaNiO_2$ with better lattice matching transformed to a-axis-orientated $LaNiO_2$ with poorer lattice matching as the reaction time or temperature increased.[26]

These results suggest that the crystal growth direction is determined by kinetics rather than by thermodynamics including epitaxial stabilization. One possible explanation is that the anisotropic diffusion of atoms promotes a specific arrangement of atoms with respect to the substrate lattice. Because the topotactic reaction on thin films mainly occurs from their surfaces, the atomic diffusion perpendicular to the film surface dominates the reaction.[27] The growth of (110) oriented $NdNiO_xH_y$, contrary to our expectation, may be the consequence of such perpendicular diffusion of the constituting atoms. Further studies on chemical transport properties such as anisotropic ionic conductivity may help to elucidate the detailed mechanisms.

Conclusions

We have investigated the soft chemical reaction of $NdNiO_3$ thin films with CaH_2. When the precursor film was reacted at 240 °C, [001]-oriented $NdNiO_xH_y$ ($x \sim 2.3$, $y \sim 0.7$) with a defect-fluorite structure was grown on a thin interfacial layer of infinite-layer $NdNiO_2$. At the elevated reaction temperature of 400 °C, we observed the growth of a [110]-oriented defect-fluorite phase, although it seemed more poorly lattice-matched to $SrTiO_3$ [100] than the [001]-oriented $NdNiO_xH_y$ did.

The incorporation of a large amount of hydrogen into the films suggests the potential of $NdNiO_x$ for hydrogen storage. Hydrogen storage using single crystals is not practical because of the small surface/volume ratio. However, they are useful for the observation of fundamental kinetics of diffusion-controlled reactions.

Acknowledgements

This work was supported by the Kurata Memorial Hitachi Science and Technology Foundation, Core Research for Evolutionary Science and Technology of Japan Science and Technology Agency, and a Grant-in-Aid for Scientific Research (No. 15H05424) from the Japan Society for the Promotion of Science (JSPS). One of the authors (TO) was supported by the Japan Society for the Promotion of Science through Program for Leading Graduate Schools (MERIT).

References

1 T. Yamamoto and H. Kageyama, *Chem. Lett.*, 2013, **42**, 946–953.
2 M. A. Hayward, in *Comprehensive Inorganic Chemistry II*, ed. J. Reedijk and K. Poeppelmeier, Elsevier, Amsterdam, 2nd edn, 2013, ch. 2.15, pp. 417–453.
3 M. A. Hayward, M. A. Green, M. J. Rosseinsky and J. Sloan, *J. Am. Chem. Soc.*, 1999, **121**, 8843–8854.
4 M. A. Hayward and M. J. Rosseinsky, *Solid State Sci.*, 2003, **5**, 839–850.
5 V. V. Poltavets, K. A. Lokshin, S. Dikmen, M. Croft, T. Egami and M. Greenblatt, *J. Am. Chem. Soc.*, 2006, **128**, 9050–9051.
6 F. D. Romero, S. J. Burr, J. E. McGrady, D. Gianolio, G. Cibin and M. A. Hayward, *J. Am. Chem. Soc.*, 2013, **135**, 1838–1844.
7 M. A. Hayward and M. J. Rosseinsky, *Chem. Mater.*, 2000, **12**, 2182–2195.
8 Y. Tsujimoto, C. Tassel, N. Hayashi, T. Watanabe, H. Kageyama, K. Yoshimura, M. Takano, M. Ceretti, C. Ritter and W. Paulus, *Nature*, 2007, **450**, 1062–1065.
9 M. A. Hayward, E. J. Cussen, J. B. Claridge, M. Bieringer, M. J. Rosseinsky, C. J. Kiely, S. J. Blundell, I. M. Marshall and F. L. Pratt, *Science*, 2002, **295**, 1882–1884.
10 Y. Kobayashi, O. J. Hernandez, T. Sakaguchi, T. Yajima, T. Roisnel, Y. Tsujimoto, M. Morita, Y. Noda, Y. Mogami, A. Kitada, M. Ohkura, S. Hosokawa, Z. Li, K. Hayashi, Y. Kusano, J. E. Kim, N. Tsuji, A. Fujiwara, Y. Matsushita, K. Yoshimura, K. Takegoshi, M. Inoue, M. Takano and H. Kageyama, *Nat. Mater.*, 2012, **11**, 507–511.

Open Access Article. Published on 01 July 2016. Downloaded on 10/20/2025 3:45:00 PM.
This article is licensed under a Creative Commons Attribution 3.0 Unported Licence.

11 F. Denis Romero, A. Leach, J. S. Möller, F. Foronda, S. J. Blundell and M. A. Hayward, *Angew. Chem., Int. Ed.*, 2014, **53**, 7556–7559.
12 M. Kawai, S. Inoue, M. Mizumaki, N. Kawamura, N. Ichikawa and Y. Shimakawa, *Appl. Phys. Lett.*, 2009, **94**, 082102, DOI: 10.1063/1.3078276.
13 D. Kaneko, K. Yamagishi, A. Tsukada, T. Manabe and M. Naito, *Phys. C*, 2009, **469**, 936–939.
14 S. Inoue, M. Kawai, Y. Shimakawa, M. Mizumaki, N. Kawamura, T. Watanabe, Y. Tsujimoto, H. Kageyama and K. Yoshimura, *Appl. Phys. Lett.*, 2008, **92**, 161911, DOI: 10.1063/1.2913164.
15 T. Matsuyama, A. Chikamatsu, Y. Hirose, T. Fukumura and T. Hasegawa, *Appl. Phys. Express*, 2011, **4**, 013001, DOI: 10.1143/APEX.4.031001.
16 T. Yajima, A. Kitada, Y. Kobayashi, T. Sakaguchi, G. Bouilly, S. Kasahara, T. Terashima, M. Takano and H. Kageyama, *J. Am. Chem. Soc.*, 2012, **134**, 8782–8785.
17 T. Katayama, A. Chikamatsu, H. Kamisaka, Y. Yokoyama, Y. Hirata, H. Wadati, T. Fukumura and T. Hasegawa, *AIP Adv.*, 2015, **5**, 107147, DOI: 10.1063/1.4935190.
18 G. Bouilly, T. Yajima, T. Terashima, Y. Kususe, K. Fujita, C. Tassel, T. Yamamoto, K. Tanaka, Y. Kobayashi and H. Kageyama, *CrystEngComm*, 2014, **16**, 9669–9674.
19 T. Katayama, A. Chikamatsu, Y. Hirose, H. Kumigashira, T. Fukumura and T. Hasegawa, *J. Phys. D: Appl. Phys.*, 2014, **47**, 135304, DOI: 10.1088/0022-3727/47/13/135304.
20 M. Imada, A. Fujimori and Y. Tokura, *Rev. Mod. Phys.*, 1998, **70**, 1039–1263.
21 M. Medarde, C. Dallera, M. Grioni, B. Delley, F. Vernay, J. Mesot, M. Sikora, J. A. Alonso and M. J. Martínez-Lope, *Phys. Rev. B: Condens. Matter*, 2009, **80**, 245105, DOI: 10.1103/PhysRevB.80.245105.
22 P.-H. Xiang, N. Zhong, C.-G. Duan, X. D. Tang, Z. G. Hu, P. X. Yang, Z. Q. Zhu and J. H. Chu, *J. Appl. Phys.*, 2013, **114**, 243713, DOI: 10.1063/1.4858455.
23 M. Stewart, J. Liu, M. Kareev, J. Chakhalian and D. Basov, *Phys. Rev. Lett.*, 2011, **107**, 176401, DOI: 10.1103/PhysRevLett.107.176401.
24 Y. Krockenberger, K. Sakuma and H. Yamamoto, *Appl. Phys. Express*, 2012, **5**, 043101, DOI: 10.1143/APEX.5.043101.
25 M. Widerøe, H. Fjellvåg, T. Norby, F. Willy Poulsen and R. Willestofte Berg, *J. Solid State Chem.*, 2011, **184**, 1890–1894.
26 M. Kawai, K. Matsumoto, N. Ichikawa, M. Mizumaki, O. Sakata, N. Kawamura, S. Kimura and Y. Shimakawa, *Cryst. Growth Des.*, 2010, **10**, 2044–2046.
27 S. Inoue, M. Kawai, N. Ichikawa, H. Kageyama, W. Paulus and Y. Shimakawa, *Nat. Chem.*, 2010, **2**, 213–217.

 This journal is © The Royal Society of Chemistry 2016